Detailed characterization of neutron-proton equilibration in dynamically deformed nuclear systems

A. Rodriguez Manso, A. B. McIntosh, A. Jedele, K. Hagel, L. Heilborn, Z. Kohley, L. W. May, A. Zarrella, and S. J. Yennello

Phys. Rev. C **95**, 044604 — Published 5 April 2017

DOI: 10.1103/PhysRevC.95.044604

Detailed characterization of neutron-proton equilibration in dynamically deformed nuclear systems

A. Rodriguez Manso[1],[*] A.B. McIntosh[1],[†] A. Jedele[1,2], K. Hagel[1], L. Heilborn[1,2], Z. Kohley[3,4], L.W. May[1,2], A. Zarrella[1,2], and S.J. Yennello[1,2]
[1]*Cyclotron Institute, Texas A&M University, College Station, Texas 77843, USA*
[2]*Chemistry Department, Texas A&M University, College Station, Texas 77843, USA*
[3]*National Superconducting Cyclotron Laboratory, Michigan State University, East Lansing, Michigan 48824, USA and*
[4]*Department of Chemistry, Michigan State University, East Lansing, Michigan 48824, USA*

(Dated: March 7, 2017)

We study neutron-proton equilibration in dynamically deformed nuclear systems by investigating the correlations between the two largest fragments produced in collisions of ^{70}Zn +^{70}Zn, ^{64}Zn +^{64}Zn, ^{64}Ni +^{64}Ni and ^{64}Zn +^{64}Ni at 35 MeV per nucleon. The extent of equilibration is investigated using the rotation angle as a clock for the equilibration. The initially dissimilar fragments converge exponentially with consistent rate constants across a wide variety of reaction partners and systems, indicating the equilibration follows first-order kinetics.

I. INTRODUCTION

The motivation for investigating the nuclear equation of state (EOS) comes from the desire to give a macroscopic description of the nucleus as a many body system and understand the thermodynamic relationships that characterize the strongly interacting nuclear matter. In particular, we aim at understanding the EOS as governing the processes related to the dynamics of heavy-ion collisions.

In this work we are interested in the aspect of the EOS associated with the asymmetry of neutrons and protons. The asymmetry energy strongly influences the location of the valley of β stability, the migration of neutrons and protons in nuclear reactions, and the structure and composition of neutron stars. The multi-neutron and multi-proton exchange between two large nuclei in heavy-ion collisions allows neutron-proton (NZ) equilibration [1–7]. The extent of equilibration can be used to constrain the density dependence of the asymmetry energy (see Ref. [8] and references therein).

Heavy-ion reactions near the Fermi energy proceed through extremely deformed intermediate states. The general features of such a reaction are illustrated in Figure 1, courtesy of Anna Poulsen [9]. Initially, there are the target and projectile (panel (*a*)) and a deeply penetrating contact between them with slight compression. Only a fraction of the energy of relative motion is converted to other degrees of freedom. As the excited Projectile-Like Fragment (PLF*) and excited Target-Like Fragment (TLF*) begin to separate from each other (panel (*b*)), a low-density neck of nuclear material is formed between them due to, in a classical description, nuclear viscosity and surface tension. Neutrons are driven preferentially to the low-density neck due to the density dependence of the asymmetry energy [10]. This is illustrated in the figure by the excess of neutrons (in blue) in the neck and the relatively higher concentration of protons (in red) in the PLF* and TLF* regions. The velocity gradient stretches the system and the competition of the velocity gradient with surface tension amplifies instabilities (panel (*c*)); analogy to the breakup of a Rayleigh jet may be appropriate [11]. The velocity gradient stretches the system beyond the capabilities of the nuclear force to hold it together and the system ruptures (panel (*d*)). After one rupture of the neck, the now separated PLF* and TLF* are likely to be strongly deformed along the separation axis and, because of their deformation, they are likely to break again. The subsequent breakup of the PLF* into two pieces (the heavy fragment, HF, and the light fragment, LF) is illustrated in panel (*e*). If some time elapses between the PLF*-TLF* scission and the HF-LF scission, the angular momentum of the PLF* causes rotation through an angle so that the relative velocity $\vec{v}_{rel}$ of HF and LF makes a non-zero angle with the PLF*-TLF* separation axis $\vec{v}_{CM}$, the center-of-mass velocity of the PLF*. If the angular velocity can be deduced and the breakup timescale is short relative to the rotational period, the rotation angle can be used as a clock. Since the neck is neutron-rich at the time of the first scission, nucleon flow between regions of the deformed PLF* allow NZ equilibration to occur between the developing HF and LF. Thus measuring the composition of HF and LF as a function of the rotation angle allows direct observation of the time dependence of NZ equilibration.

In the late ′70s and early ′80s, the timescale of NZ equilibration between projectile and target was assessed using a rotation angle technique and determined to be on the order of 1 zs [12–17]. Recently this idea has been revived to investigate equilibration within a deformed PLF*. For different ranges of rotation angle, a clear generally decreasing trend of the neutron-richness of the LF is observed, and a timescale is obtained [18–21]. In [22] we have reported high-resolution characterization of NZ equilibration by measuring the composition of the

---

[*] alisrodriguezmanso87@gmail.com
[†] alan.b.mcintosh@gmail.com

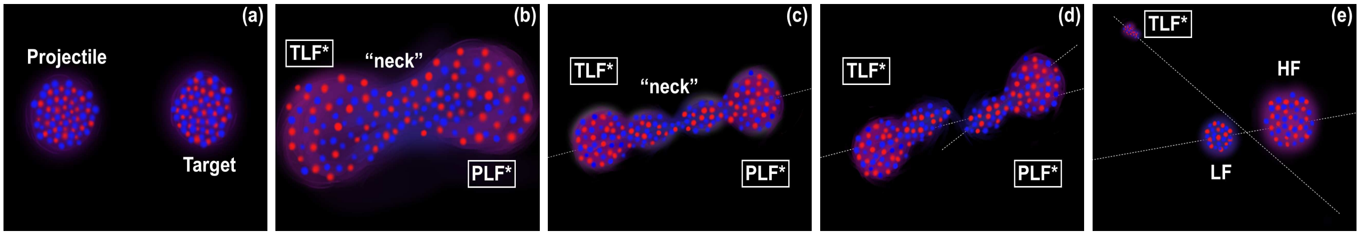

FIG. 1. Cartoon representation of dynamical deformation and decay. Panel (*a*) shows a projectile approaching target. In panel (*b*), the projectile rotated around the target forming a low-density “neck” region. In panel (*c*), the excited PLF* and TLF* have moved further away from each other and stretched into a “string of pearls” with the smallest fragments forming out of the neck region. Panel (*d*) represents the breaking of the nuclear system with the PLF* separating from the TLF*. Panel (*e*) shows the subsequent separation of the PLF* into HF and LF. (color online) (Cartoon figures from Anna Poulsen `https://oxidantshappencomics.wordpress.com`)

HF and LF with sufficiently high angular resolution to demonstrate an exponential dependence of the composition with time, indicative of first-order kinetics.

In this paper, we increase the breadth and depth of our previous high-resolution coincidence measurement. In Section II we briefly review the experimental setup and analysis details of the specific reactions studied. Section III is focused on the discussion of the results obtained. Finally, we summarize our conclusions in Section IV.

II. EXPERIMENT AND EVENT SELECTION

The experiment consisted of beams of ^{70}Zn, ^{64}Zn and ^{64}Ni accelerated to 35 MeV/nucleon by the K500 Cyclotron at Texas A&M University which were focused onto thin foils of ^{70}Zn, ^{64}Zn and ^{64}Ni to obtain symmetric and asymmetric systems. The products of the reactions were measured in the Neutron Ion Multi-detector for Reaction Oriented Dynamics (NIMROD) [23]. We performed simultaneous measurement of both partners of a binary split of the PLF*. NIMROD provides excellent isotopic resolution to identify charged particles at least up to $Z = 17$ in the detector telescopes [24, 25]. In addition, NIMROD provides almost complete geometric coverage over the angular range from 3.6° to 167°. NIMROD has excellent efficiency for measuring the fast-moving decay products of the PLF* and the neck region, but thresholds prevent the identification of sizable fragments from the TLF*. We take advantage of the strengths of the data set, focusing on the binary decay of the PLF* into two major fragments.

As in [22], events are selected that have at least two charged particles measured in NIMROD. Fragments are sorted by their atomic numbers. The fragment with the largest atomic number is referred to as the “heavy fragment” (HF), while the fragment with the second largest atomic number is referred to as the “light fragment” (LF). Identical charge fragments are sorted by mass number. The HF and LF are required to have an atomic number $Z_H \geq 12$ and $Z_L \geq 3$ respectively and the total measured charge is required to be between $21 \leq Z_{Total} \leq 32$. Both the HF and LF are required to be isotopically identified.

Three combinations of HF and LF are chosen as example cases throughout much of this paper. The combinations chosen are (Z_H=14, Z_L=5), (Z_H=14, Z_L=7) and (Z_H=12, Z_L=7). These combinations allow one to examine the effect of varying Z_H and Z_L independently. The general features seen for these combinations are representative of all those seen in the experimental data.

III. RESULTS AND DISCUSSION

The fragments’ velocity distributions in the direction of the beam are used to establish the specific fragments that correspond to the PLF* daughters. Figure 2 illustrates the normalized yield as a function of the velocity distributions for the HF (in red) and the LF (in blue) in the direction of the beam for a representative system. The distributions shown are from the symmetric ^{70}Zn $+^{70}$Zn system for the three representative combinations of HF and LF: Z_H=14, Z_L=5 (upper panel), Z_H=14, Z_L=7 (middle panel) and Z_H=12, Z_L=7 (lower panel). The dashed lines (from right to left) correspond to the beam velocity (i.e v=0.27c) and half of the beam velocity or mid-velocity (i.e. v=0.13c), respectively. The LF is produced at velocities higher than mid-velocity and lower than the HF, which is produced closer to the beam velocity. Both the HF and LF are peaked well above mid-velocity which indicates that both HF and LF originate from the PLF*. This behavior is consistent for the other systems studied.

Figure 3 shows the normalized angular distributions in terms of the alignment angle (α), the in-plane angle (φ_{in}) and the out-of-plane angle (θ_{out}) in the upper left, upper right and bottom left panels, respectively. The angle α=acos$(\frac{\vec{v}_{cm}\cdot\vec{v}_{rel}}{|\vec{v}_{cm}||\vec{v}_{rel}|})$, where $\vec{v}_{cm}$=$(m_{HF}\vec{v}_{HF} + m_{LF}\vec{v}_{LF})/(m_{HF} + m_{LF})$ is the two fragments’ center of mass velocity and $\vec{v}_{rel}$=$\vec{v}_{HF} - \vec{v}_{LF}$ represents the two fragments’ relative velocity. The reaction plane is defined as the plane containing the beam axis and the two fragments’ (i.e. HF, LF) center of mass velocity ($\vec{v}_{cm}$).

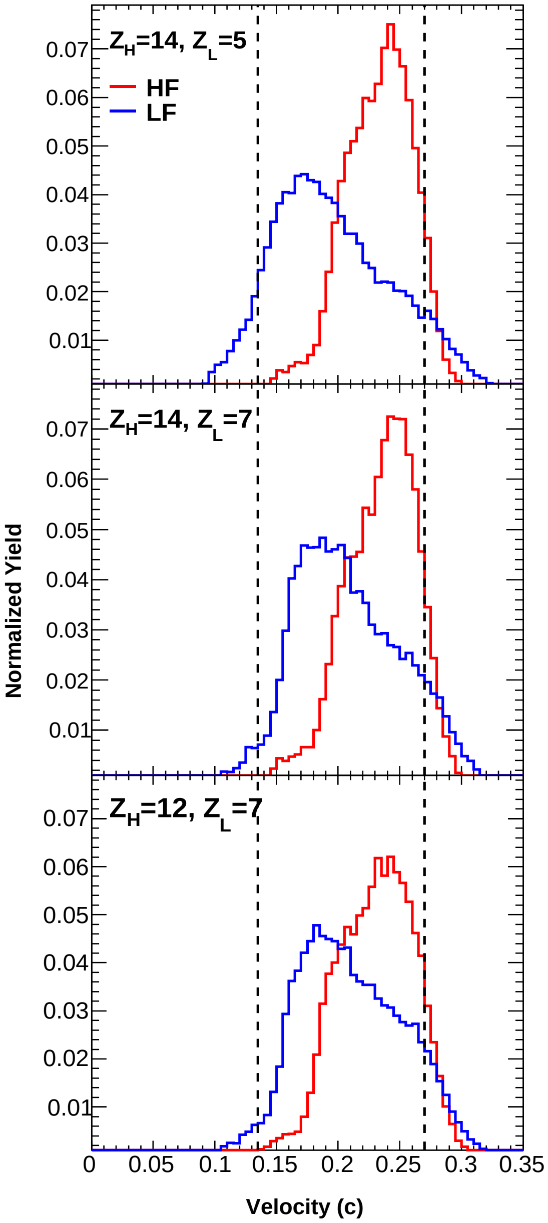

FIG. 2. Normalized velocity distributions for the HF and the LF in the direction of the beam. The HF is represented in red and the LF in blue. The distributions correspond to the ^{70}Zn +^{70}Zn system for three representative combinations of HF and LF: Z_H=14, Z_L=5 (upper panel), Z_H=14, Z_L=7 (middle panel) and Z_H=12, Z_L=7 (lower panel). The dashed vertical lines (from right to left) correspond to the beam velocity (i.e 0.27c) and mid-velocity (i.e. 0.13c), respectively. (color online)

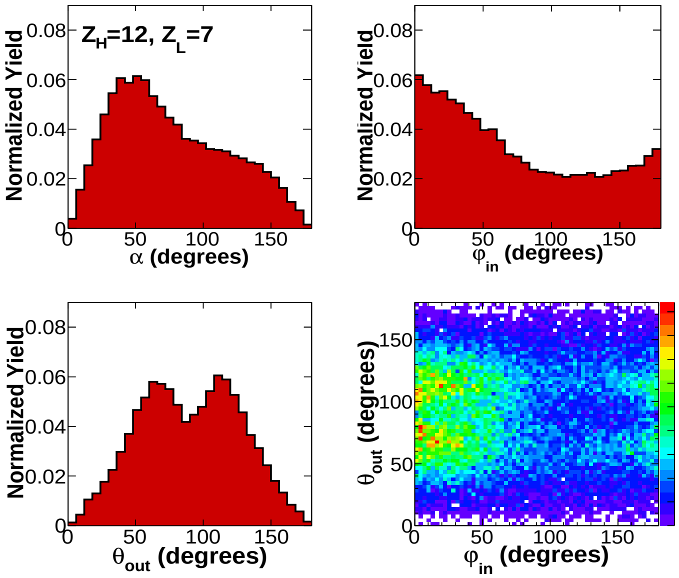

FIG. 3. Normalized yield as a function of the angular in-plane distribution φ_{in} (top right panel), out-of-plane distribution θ_{out} (bottom left panel) and α (top left panel). The bottom right panel shows the angular distribution as a function of the in-plane and out-of-plane angles simultaneously, with a linear color scale. All angular distributions shown correspond to the Z_H=12, Z_L=7 combination of HF and LF of the ^{70}Zn +^{70}Zn system. (color online)

A value of θ_{out}=90° indicates emission in the reaction plane, while 0° and 180° indicate emission perpendicular to the reaction plane. A value of φ_{in}=0° is needed for completely aligned breakup with the HF forward of the LF, and a value of φ_{in}=180° is needed for completely aligned breakup with the LF forward of the HF. The bottom right panel shows the angular distribution as a function of the in-plane and out-of-plane angles simultaneously. All angular distributions shown correspond to the Z_H=12, Z_L=7 combination of HF and LF of the symmetric ^{70}Zn +^{70}Zn system and are representatives of all systems studied.

The observed angular distributions are consistent with a significant amount of dynamical decay (i.e. the yield is concentrated in an angular range with the LF produced between the HF and the TLF*)[26–29]. Statistical decay would show a symmetric distribution of α centered at 90° and would be sinusoidal for zero spin. Higher spin would make this distribution less peaked in the middle and increase yield toward 0° and 180°, symmetrically. The in-plane angle φ_{in} would be flat for statistical decay regardless of angular momentum. The fact that α exhibits a strong peak far from 90° and that φ_{in} exhibits a peak at zero indicates a large yield of non-statistical decay. The two-dimensional plot on the bottom right panel of Figure 3 shows some interesting features that are consistent with these observations. The distribution of φ_{in} for θ_{out} near 70° or 110° is strongly peaked. The distribution of φ_{in} for θ_{out} near 30° or 150° is much flatter. This demonstrates that the dynamical yield is preferentially closer to the plane, as expected. The gap near θ_{out}=90° corresponds to the efficiency issue that is manifest at α=0° and α=180°. Both φ_{in} and α are reasonable starting points to extract information about the breakup

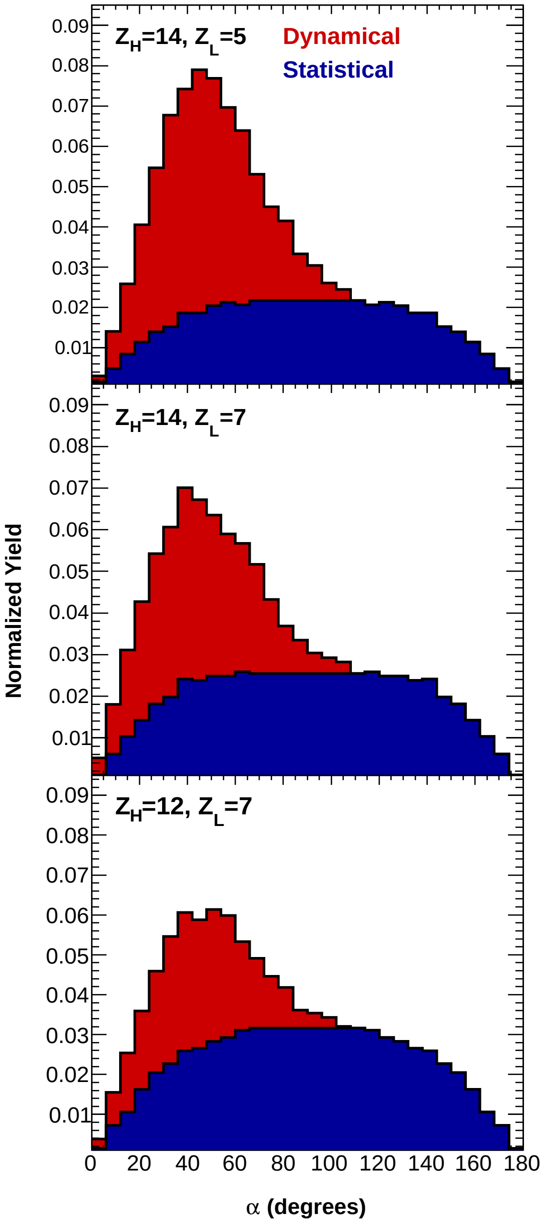

FIG. 4. Normalized angular distribution α for the ^{70}Zn +^{70}Zn system. Three representative combinations of HF and LF are shown: Z_H=14, Z_L=5 (upper panel), Z_H=14, Z_L=7 (middle panel) and Z_H=12, Z_L=7 (lower panel). The blue area represents the statistical contribution and the remaining area (red) represents the dynamical contribution. (color online)

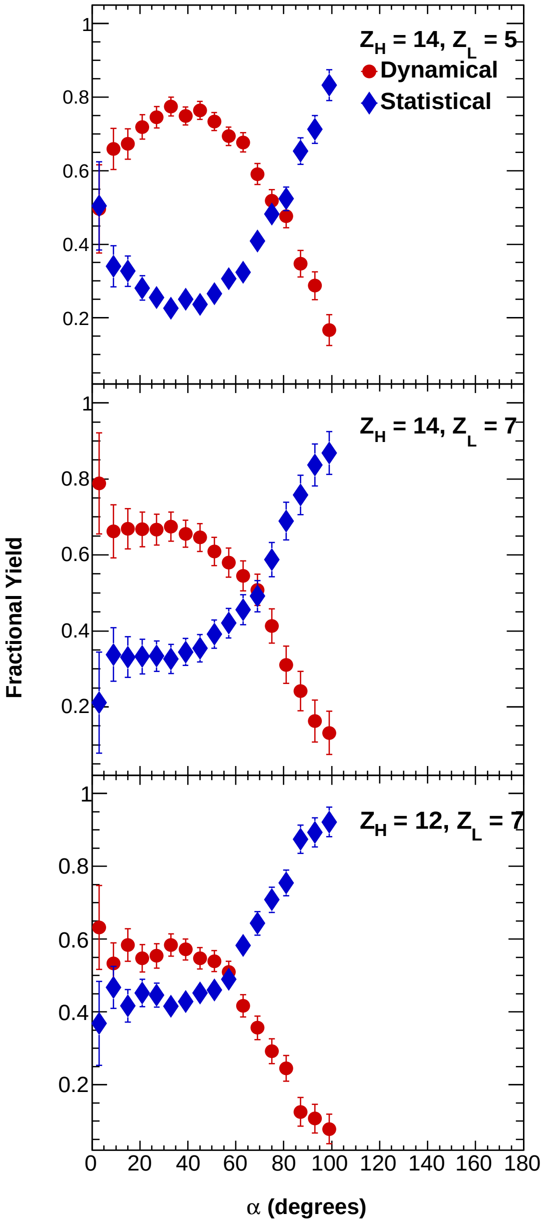

FIG. 5. Fractional yield as a function of α for the ^{70}Zn +^{70}Zn system. Three representative combinations of HF and LF are shown: Z_H=14, Z_L=5 (upper panel), Z_H=14, Z_L=7 (middle panel) and Z_H=12, Z_L=7 (lower panel). The circular red markers correspond to the dynamical contribution while the blue rhombic markers represent the statistical contribution. (color online)

alignment of the PLF*. Since the breakup of the PLF* does not have to be perfectly in the reaction plane, α seems the more reasonable choice since it describes the breakup orientation rather than a projection of it. We will revisit this point in Figure 8 when discussing the sensitivity of the composition to these two angles.

To study the PLF* deformation's alignment, representative angular distributions α are illustrated in Figure 4 for the ^{70}Zn +^{70}Zn system. The three representative combinations of HF and LF are shown. The angular distributions are not symmetric, though they are unimodal. They are strongly peaked with $\alpha < 90°$. The distributions fall toward zero at $\alpha = 0°$ and $\alpha = 180°$. This last fact is a consequence of the geometry of the detector array which gives a reduced detector efficiency (i.e. two particles incident on the same detector elements are not resolvable). This impacts particles at a particular angle α the same regardless of the mechanism of their origin.

The total yield can be understood as arising from two different mechanisms of production: statistical decay and dynamical decay. The observed yield for $\alpha > 90°$ comes primarily from statistical decays from a rotating source which produces an angular distribution that is symmetric about 90°. The excess observed yield for $\alpha < 90°$ is consistent with dynamical decay, most probable at the smallest angles and steadily decreases in probability with increasing angle. Furthermore, the excess of the observed yield for $\alpha < 90°$ is also consistent with an angular distribution peaked for the most strongly aligned configuration which corresponds to the most asymmetric splits (i.e. Z_H=14, Z_L=5), as shown in the upper panel of Figure 4. The asymmetric splits undergo shorter decay times. This is in line with observations in previous works [30, 31] where a correlation is observed between the size asymmetry of the dynamically splitting system and the width of the angular distribution. The width is understood in terms of the viscosity and bulk rearrangement, giving rise to a longer fission timescale for more symmetric splits.

In order to disentangle dynamical from statistical decay contributions, we describe the total yield as the sum of the statistical and dynamical components Y_{total}=Y_{dyn} + Y_{stat}. We assume the statistical yield is symmetric at about 90°. In addition, we also assume that the yield at large α (above 108°) is entirely statistical. This treatment implies that the efficiency of the NIMROD is the same for forward and backward emission, which we have verified with a software replica of the detector array. Modeling the precise shape of the statistical component requires a detailed knowledge of the angular distribution of intermediate-mass fragments statistically emitted from a large nucleus for a range of angular momenta. We use instead our estimate of the statistical yield based on the measured yield for large α to show that our subsequent equilibration results are quite insensitive to the accounting of statistical decay, a point to which we will return in detail in our discussion of Figure 7. Our estimates of the statistical angular distribution are shown in blue in Figure 4. The red area in the figure corresponds to the dynamical contribution.

Figure 5 shows the fractional yield as a function of the angular distribution α for the ^{70}Zn +^{70}Zn system. The three representative combinations of HF and LF are shown. The red circular markers correspond to the dynamical contribution while the blue rhombic markers represent the statistical contribution. At small angles, dynamical decay dominates the yield. As the alignment angle increases, the dynamical yield becomes less probable relative to the statistical yield. Around 60° or 80° (depending on the size asymmetry of the split) the statistical and dynamical yields become equally probable. Beyond this, the dynamical yield continues to decrease in relative yield and statistical decay dominates.

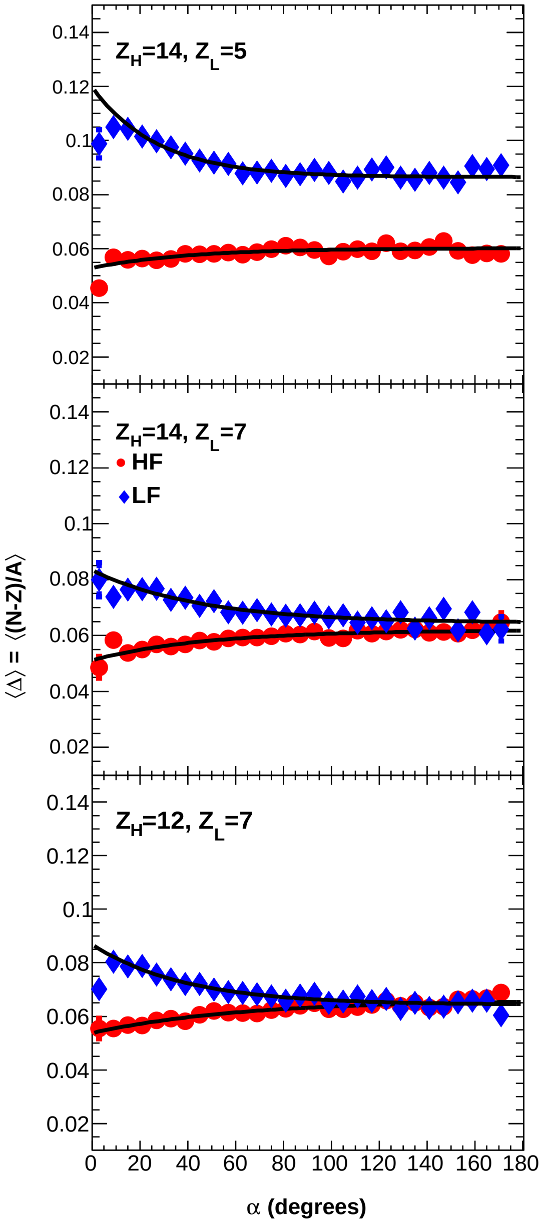

FIG. 6. Average composition $\langle\Delta\rangle$ as a function of the decay alignment α for the ^{70}Zn +^{70}Zn system. Three representative combinations of HF (red circles) and LF (blue rhombi) are shown: Z_H=14, Z_L=5 (upper panel), Z_H=14, Z_L=7 (middle panel) and Z_H=12, Z_L=7 (lower panel). The black lines correspond to the exponential fits of the data. (color online)

The average composition or asymmetry $\langle\Delta\rangle$=$\langle(N-Z)/A\rangle$ as a function of the alignment angle α is depicted in Figure 6. The figure shows the three representative combinations for the symmetric system ^{70}Zn +^{70}Zn for both HF (in red circles) and LF (in blue rhombi). The angular evolution for both the HF and the LF appears to be exponential. We parametrize the data with the form:

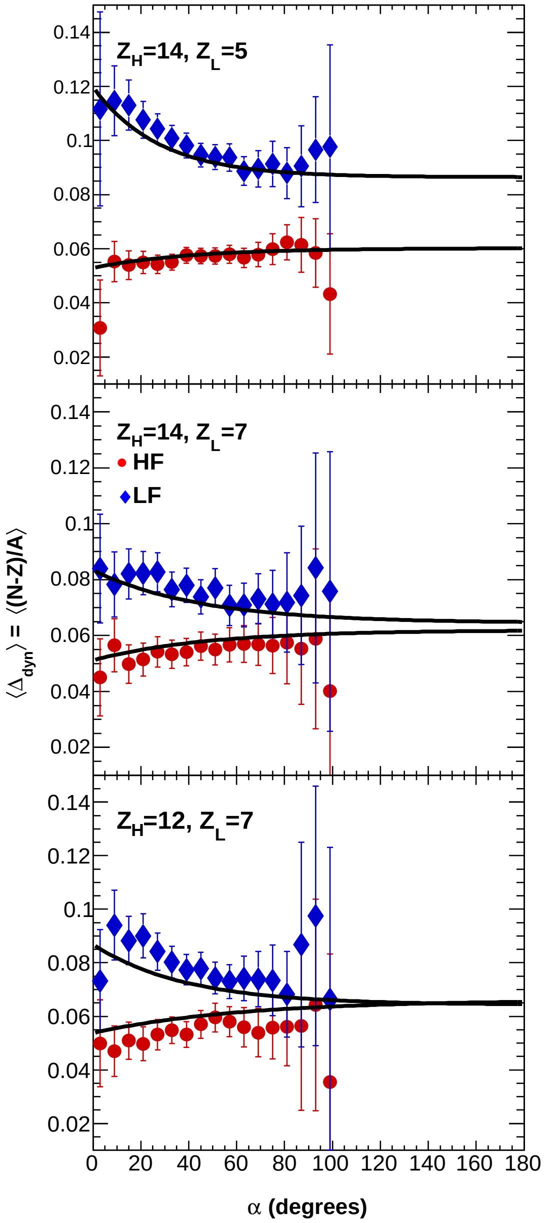

FIG. 7. Average dynamical composition, $\langle\Delta_{dyn}\rangle$, as a function of the decay alignment α for the ^{70}Zn +^{70}Zn system. Three representative combinations of HF (red circles) and LF (blue rhombi) are shown: Z_H=14, Z_L=5 (upper panel), Z_H=14, Z_L=7 (middle panel) and Z_H=12, Z_L=7 (lower panel). The black lines correspond to the exponential fit of the average composition as a function of the decay alignment. (color online)

$$\langle\Delta\rangle = a + be^{(-c\alpha)} \tag{1}$$

These fits are shown by the black lines in Figure 6 and describe the experimental data, suggesting first-order kinetics. For the moment we consider the parameterizations as guides to the eye, and will return later to the meaning of the fit parameters. The majority of the equilibration appears to be between 0° and 80°. The composition of the HF and LF evolve at comparable rates and in opposite directions as a function of the alignment-angle clock. As in [22], this represents the strongest evidence to date that the NZ equilibration can occur within a deformed nucleus and enables us to study the detailed time-dependence of the equilibration.

To investigate the impact of statistical yield on the trends observed in Figure 6, we present a method to extract the dynamical composition as a function of α. We describe the observed composition as a combination of the composition of the dynamical component and the statistical component, each weighted by their fractional yield as $\langle\Delta\rangle$=$\langle\Delta_{stat}\rangle.f_{stat}$ + $\langle\Delta_{dyn}\rangle.f_{dyn}$. We observe that the composition of the statistical component is independent of the angle for $\alpha > 100°$, and assume that this is true also for $\alpha < 100°$. This enables us to calculate $\langle\Delta_{dyn}\rangle$ as a function of α, which we present in Figure 7. The error bars depicted here reflect the statistical errors on the raw yield propagated appropriately; systematic uncertainty due to the assessment of the fractional yields has not been calculated. The exponential fits from Figure 6 are reproduced in Figure 7 for easy visual comparison. The dynamical yield generally follows the same trend as the overall yield. The compositions are slightly more extreme for the purely dynamical component (i.e. the LF is slightly more neutron-rich and the HF is slightly more neutron-poor). It is not surprising that a statistical "background" of constant composition would mute the signal present in the purely dynamical. Applying this correction to isolate the dynamical component results in significantly larger uncertainties. The rate of change of the composition is essentially unaffected by the correction and the precise values of the composition are modified slightly. We continue the analysis on the inclusive composition rather than the dynamical, with the knowledge that the rates extracted are minimally impacted by the statistical contribution, and our resulting uncertainties are minimized by avoiding the systematic uncertainty introduced by the subtraction.

In both Figures 6 and 7, the LF, which originates close to the neck region and therefore is neutron-rich, starts off with a large initial composition $\langle\Delta\rangle$ for small alignment angles. On the other hand the HF, which originates far from the neck region and therefore is neutron-poor, starts off with a small initial composition $\langle\Delta\rangle$ for small alignment angles. As the angle of rotation increases, surface tension drives the system towards sphericity, keeping the HF and LF in contact longer and consequently, having more time to exchange nucleons. The opportunity to exchange nucleons allows the asymmetry energy to drive a net neutron flow out of the LF and into the HF to equilibrate the chemical potentials of the two nascent fragments, giving rise to similar values of the composition for the LF and the HF at higher alignment values. The $\langle\Delta_L\rangle$ changes by a larger amount than the $\langle\Delta_H\rangle$. This is

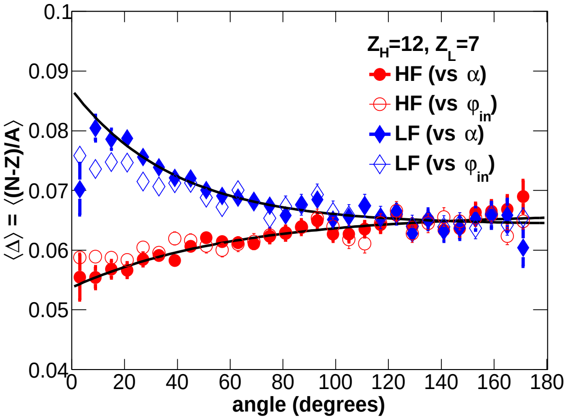

FIG. 8. Average composition $\langle\Delta\rangle$ as a function of the decay alignment α (in full markers) and the in-plane angle φ_{in} (in open markers) for the Z_H=12, Z_L=7 pair in the ^{70}Zn $+^{70}$Zn system. (color online)

largely a consequence of the mass conservation, considering that the heavy fragment is larger with respect to the light one and thus, the exchange of nucleons affects the composition of the latter more.

In Figure 3, the dynamical yield was observed in terms of the alignment angle α and the in-plane angle φ_{in}. The composition as a function of α and the composition as a function of φ_{in} (in full and open markers respectively) are compared in Figure 8. The figure depicts the Z_H=12, Z_L=7 pair for the symmetric system ^{70}Zn $+^{70}$Zn, and again the exponential fits from Figure 6 are reproduced for comparison. Since the rotation of the PLF* as it decays into HF and LF is predominantly around an axis perpendicular to the reaction plane, we expect the composition as a function of these two angles to be similar. However, since the rotation axis can be somewhat canted from perpendicular, we expect that α would provide a truer measure of the time. The projection onto the reaction plane required to obtain φ_{in} causes a smearing in angle, dependent on how canted the rotation axis is, and thus reduces the observed dependence. Indeed this is manifest in Figure 8. While both angles are sensitive observables for the reaction time, α shows the stronger sensitivity. In fact, since the dependence of the composition on angle cannot be manufactured (for example by statistical decay), the angle with the strongest dependence is the most suitable angle to use as the clock.

For completeness, Figure 9 shows all the combinations of Z_H and Z_L used in the analysis of the symmetric system ^{70}Zn $+^{70}$Zn. In the horizontal direction (from left to right) Z_L increases, while in the vertical direction (from top to bottom) the Z_H increases. The black curves show exponential fits to the data in each panel. Where no fits are shown, the data did not support reasonable convergence of at least one of the two exponential fits (within the ROOT MINUIT package).

In all the combinations studied, as α increases, the $\langle\Delta\rangle$ value decreases for the LF and rises for the HF, with all pairs showing exponential trends, or consistent with an exponential trend within uncertainties. Moreover, the exponential rises and falls all appear to occur on similar time scales. Even when fits fail to reproduce the data, due to low statistics, the trends for Z_H and Z_L are still observable (e.g. combination Z_H=14, Z_L=9). In general, trends for a given Z_L are seen for all pairings of that Z_L, where the magnitude of change in the $\langle\Delta\rangle$ value, within a Z_L, is the same regardless of Z_H. Similarly, trends for a given Z_H are seen for all pairings of that Z_H, where the magnitude of change in the $\langle\Delta\rangle$ value, within a Z_H, is the same regardless of Z_L.

In the decaying PLF*, the local composition is influenced by the local chemical potential. Following scission of the PLF* into the HF and LF, the HF and LF may be in excited states which may undergo light particle secondary decay (mostly n, p and α particles). The final state composition is influenced by the initial composition and by the ground state binding energies of the available daughter nuclei. Given that secondary decay can modify the composition we observe, it is important to note two things. First, the crossing of the $\langle\Delta_L\rangle$ and $\langle\Delta_H\rangle$ does not necessarily contain any more physical meaning than that secondary decay must be considered. Second, secondary decay is independent of the breakup orientation α, and thus is only able to mute or destroy the $\langle\Delta\rangle$ as a function of α dependence, not create one.

We explore the impact of secondary decay on the composition and alignment angle correlation with the statistical decay code GEMINI++ [32]. Nuclei with Z=7, 8, 9, 10 are de-excited with GEMINI++. The initial mass number A is determined from the initial atomic number Z and initial composition $\langle\Delta\rangle$. The initial $\langle\Delta\rangle$ is given an arbitrary but reasonable dependence on the angle α. For every α, $\langle\Delta\rangle$ is sampled from a distribution with mean μ (which depends on α) and with standard deviation σ=0.1. The correlation between $\langle\Delta\rangle$ and α prior to secondary decay is shown by the solid markers in Figure 10. These starting points are arbitrary. The main idea is to observe the effects of secondary decay given known starting points. The upper panel shows the effects of varying the initial excitation energy from 1 MeV/nucleon to 2 MeV/nucleon. The average composition $\langle\Delta\rangle$ of the final state fragments that have a Z=7 is shown by the open markers for 1 MeV/nucleon (blue circles) and 2 MeV/nucleon (red squares). In both cases, the exponential dependence is maintained with essentially the same rate constant, but there is a shift to lower composition and a muting of the amplitude of the trend. The shift and muting is stronger for higher excitation energy as expected. The trend is not destroyed or created, and the characteristic rate of the exponential is retained. The equilibrium value is 0.6 and 0.5 for the two cases, indicating an average composition near ^{15}N with slightly more ^{14}N than ^{16}N, as expected. The lower panel of Figure 10 shows the effect of varying the starting $\langle\Delta\rangle$ on the final $\langle\Delta\rangle$. Again, the initial composition

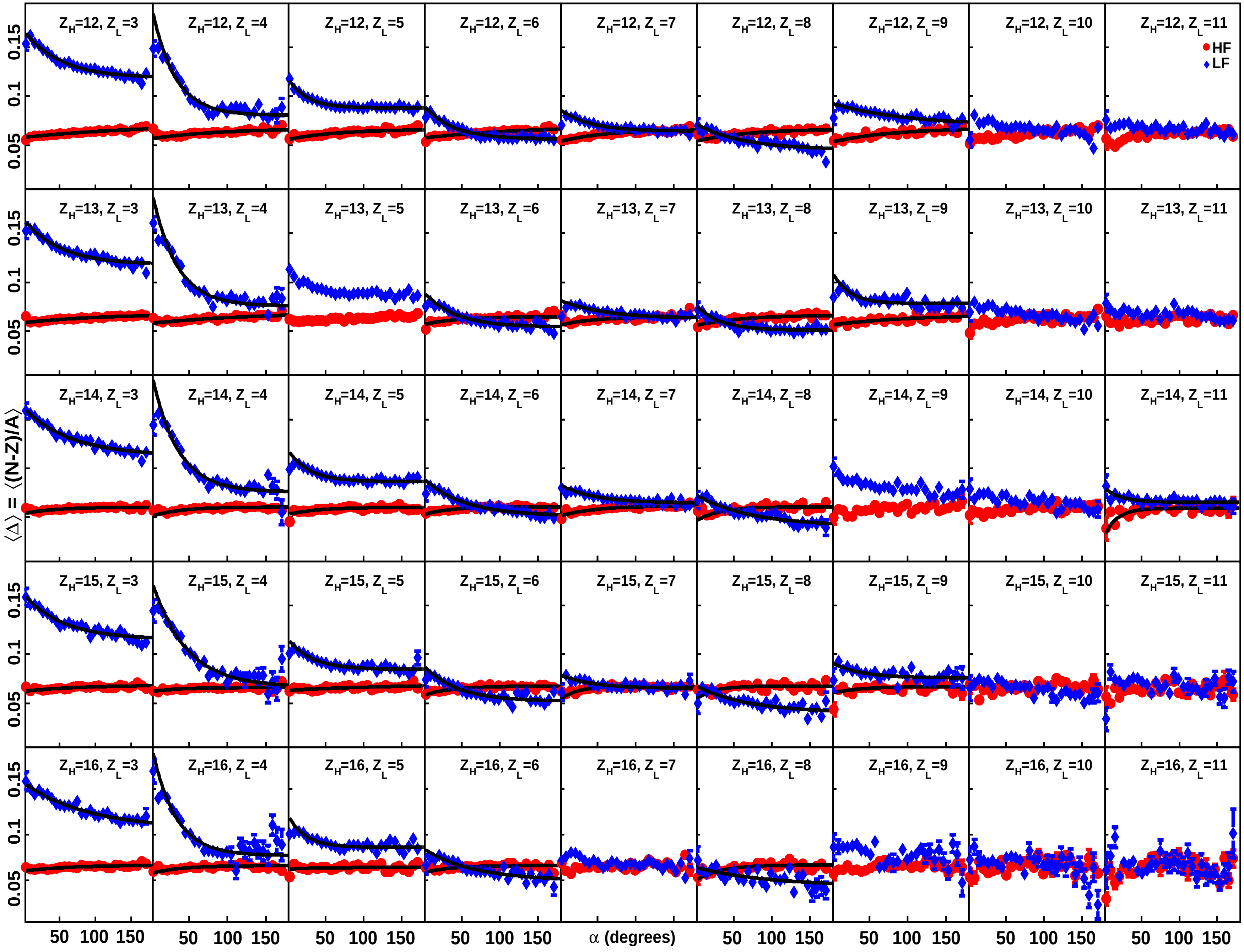

FIG. 9. Average composition $\langle\Delta\rangle$ as a function of the decay alignment α in all thirty-two combinations used in the analysis of the ^{70}Zn $+^{70}$Zn system. The HF is shown in red circles and the LF in blue rhombi. The black lines show exponential fits to the data, only for those Z_H, Z_L pairs for which both fits converge. (color online)

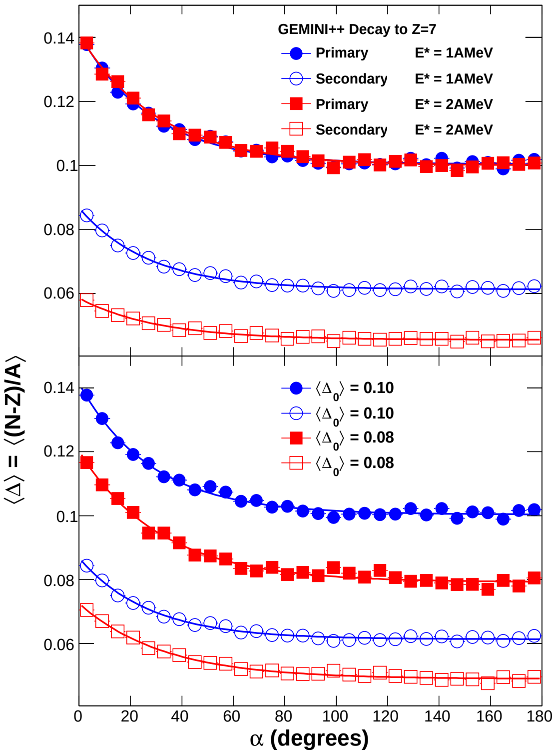

FIG. 10. GEMINI++ simulations show the effects of secondary decay on the composition $\langle\Delta\rangle$ as a function of the alignment angle α. Full markers show initial composition and open markers show the composition after secondary decay. Upper panel show the effect of varying the excitation energy from 1AMeV (blue circles) to 2AMeV (red squares). Lower panel shows the effect of varying the initial composition from neutron-rich (blue circles) to less neutron-rich (red squares). (color online)

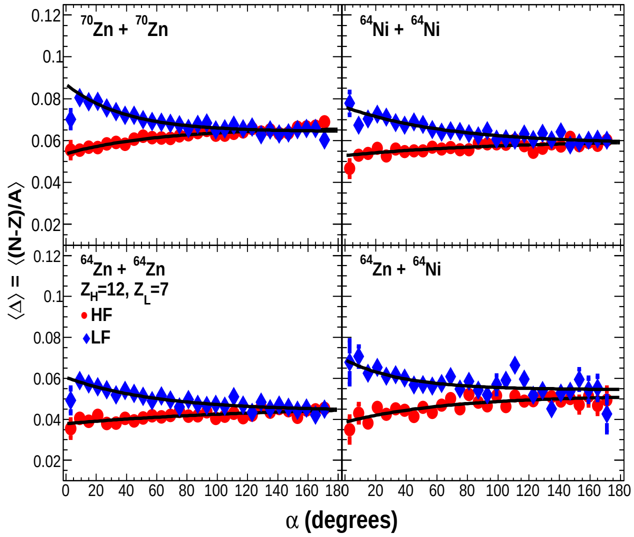

FIG. 11. Average composition $\langle\Delta\rangle$ as a function of the decay alignment α for the Z_H=12, Z_L=7 pair in all systems studied (i.e. ^{70}Zn +^{70}Zn, ^{64}Zn +^{64}Zn, ^{64}Ni +^{64}Ni and ^{64}Zn +^{64}Ni). The HF is represented in red circles and the LF in blue rhombi. The black lines correspond to the exponential fits of the data. (color online)

and alignment angle correlations are shown, though the mean changes with α, the width of the Gaussian sampled for $\langle\Delta\rangle$ does not depend on α and remains set at 0.1. The system with the initially larger asymmetry is shifted down more strongly by secondary decay. This is not surprising since a system farther from the valley of stability feels a stronger force driving it back toward the valley. However, even after secondary decay, the more neutron-rich system clearly remains more neutron-rich. Importantly, once again the rate of the characteristic exponential is retained. We summarize our study of secondary decay by saying that this process does not create the composition and alignment angle dependence, nor is able to destroy it. The dependence is muted but preserved, and the rate of the exponential is not appreciably affected. We also note that since the ground state binding energies appear to be an attractor in this mass region, it is not surprising that in Figure 9 gaps or crossings of $\langle\Delta_H\rangle$ and $\langle\Delta_L\rangle$ are observed. The actual values of $\langle\Delta\rangle$ in these cases are not the most interesting quantity, rather it is the change, particularly the rate of change, that we are interested in and able to characterize.

So far we have focused on results from collisions of ^{70}Zn +^{70}Zn. We now expand our study to other projectiles and targets. The fits of $\langle\Delta\rangle$ as a function of α are performed for thirty-two pairings of Z_H and Z_L for the ^{70}Zn +^{70}Zn and the ^{64}Zn +^{64}Zn systems, for twenty-five pairings for the ^{64}Ni +^{64}Ni system and for sixteen pairings for the ^{64}Zn +^{64}Ni asymmetric system. Figure 11 shows the average composition $\langle\Delta\rangle$ as a function of the decay alignment α for the Z_H=12, Z_L=7 pair in all the systems studied: ^{70}Zn +^{70}Zn (top left) , ^{64}Zn +^{64}Zn (bottom left), ^{64}Ni +^{64}Ni (top right) and ^{64}Zn +^{64}Ni (bottom right). From the comparison of the different panels it is observed that HF and LF for the ^{70}Zn +^{70}Zn and ^{64}Ni +^{64}Ni systems have $\langle\Delta\rangle/\alpha$ correlations that are essentially the same. The ^{64}Zn + ^{64}Zn is less neutron-rich than the other two symmetric systems. We see that the $\langle\Delta\rangle/\alpha$ correlation is shifted to lower values (i.e. lower equilibrium composition) but the rate constant and the change from initial to final value (i.e. b parameter) are essentially the same. The comparison between the ^{64}Zn +^{64}Zn and the ^{64}Zn +^{64}Ni systems is quite interesting. The initial composition for the HF is essentially the same for the two, but the composition of the LF is significantly more neutron-rich for the system with the more neutron-rich target. For both systems, the composition of HF and LF approach a common value, but this value is more neutron-rich for the system with the neutron-rich target. While the magnitude of these shifts is not far from the statistical errors on each individual point, the systematic shift of all the points from one system to the other is con-

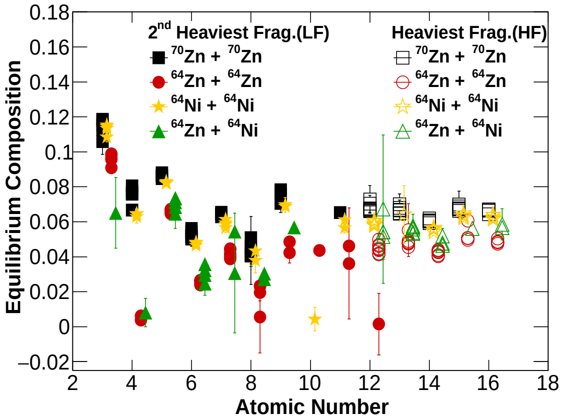

FIG. 12. Equilibrium composition as a function of the atomic number. All four systems are represented: ^{70}Zn +^{70}Zn in black squares, ^{64}Zn +^{64}Zn in red circles, ^{64}Ni +^{64}Ni in yellow stars and ^{64}Zn +^{64}Ni in green triangles. The open markers correspond to the atomic numbers of the HF and the full markers represent the atomic numbers of the LF. The different sets of data are slightly horizontally offset for clarity. (color online)

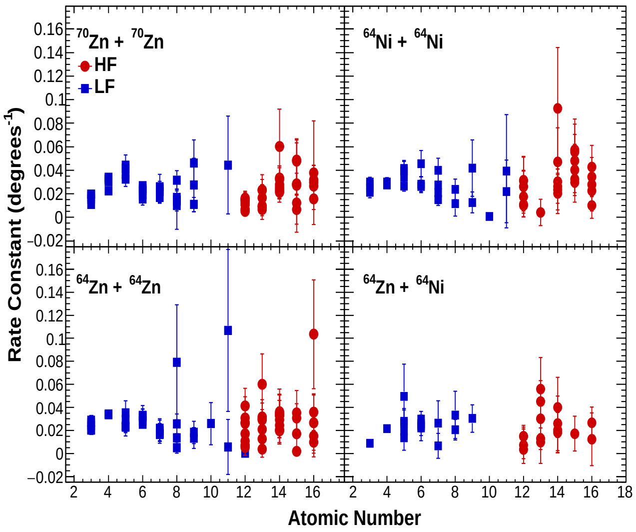

FIG. 13. Rate constants (in units of inverse degrees) as a function of the atomic number. All four systems are represented: ^{70}Zn +^{70}Zn (top left panel), ^{64}Ni +^{64}Ni (top right panel), ^{64}Zn +^{64}Zn (lower left panel) and ^{64}Zn +^{64}Ni (lower right panel). The red circles represent the atomic numbers of the HF while the blue squares represent the atomic numbers of the LF. (color online)

sistent with the expected effects of changing the neutron richness of the target.

In the exponential fits throughout this paper from Eq.1, the parameter a is the equilibrium composition and c (i.e. the exponential slope) is a surrogate of the rate constant for equilibration. Figure 12 shows the equilibrium composition as a function of the atomic number for the ^{70}Zn +^{70}Zn, the ^{64}Zn +^{64}Zn, the ^{64}Ni +^{64}Ni and the ^{64}Zn +^{64}Ni systems, in black squares, red circles, yellow stars and green triangles, respectively. The open markers correspond to the atomic numbers of the HF while the full markers represent the atomic numbers of the LF. The error bars reflect the uncertainty due to the fitting procedure. The x positions of the points in the graphs are offset slightly differently for each system in order to facilitate visualization of the results.

It is observed that the equilibrium composition starts off showing the higher values for the lightest fragments, while decreasing in magnitude for the higher Z_L values until a plateau is reached for the heaviest fragments, Z_H. While looking at the ^{70}Zn +^{70}Zn system (black squares), both the Z_L and the Z_H points are narrowly clustered, indicating that the equilibrium value for the LF depends on Z_L but not on Z_H and similarly for the HF, the equilibrium value depends on Z_H but not on Z_L. This is consistent with dependence on available isotopes for that specific Z_L or Z_H. Such interpretation holds for the other systems studied.

While comparing the ^{70}Zn +^{70}Zn system (in black squares) and the ^{64}Ni +^{64}Ni system (in yellow stars), which have similar neutron-rich system composition, the systems show approximately the same equilibrium composition for all their daughters. The ^{64}Zn +^{64}Zn system (in red circles), which has less neutrons overall, has consistently less neutron-rich equilibrium compositions for all its daughters. On average the asymmetric system (^{64}Zn +^{64}Ni in green triangles) has slightly more neutron-rich daughters than the neutron-poor system and slightly less neutron-rich daughters than the neutron-rich system. Although the error bars are in several cases significant, this systematic behavior is consistent with the expected effect of the neutron-rich target ^{64}Ni. This behavior is also consistent with the target effect observed in [19].

Figure 13 shows the rate constants (in units of inverse degrees) as a function of the atomic number for the ^{70}Zn +^{70}Zn (top left panel), ^{64}Ni +^{64}Ni (top right panel), ^{64}Zn +^{64}Zn (lower left panel) and ^{64}Zn +^{64}Ni (lower right panel) systems. The red circles represent the atomic numbers of the HF while the blue squares represent the atomic numbers LF. The error bars denote the uncertainty from the fitting procedure. The rate constant is the relevant parameter to calculate the equilibration times, as in [22]. These rate constants for LF at any given Z_L do not show any statistically significant dependence on Z_H. Similarly, the rate constants for HF at any given Z_H do not show any statistically significant dependence on Z_L. The average rate constant in units of inverse degrees for the LF is 0.03 ± 0.01 in all the symmetric systems studied while for the HF is 0.02 ± 0.01, 0.03 ± 0.01 and 0.03 ± 0.01 in the ^{70}Zn +^{70}Zn, ^{64}Zn +^{64}Zn and ^{64}Ni +^{64}Ni systems, respectively. In the case of the asymmetric system ^{64}Zn +^{64}Ni, the average rate con-

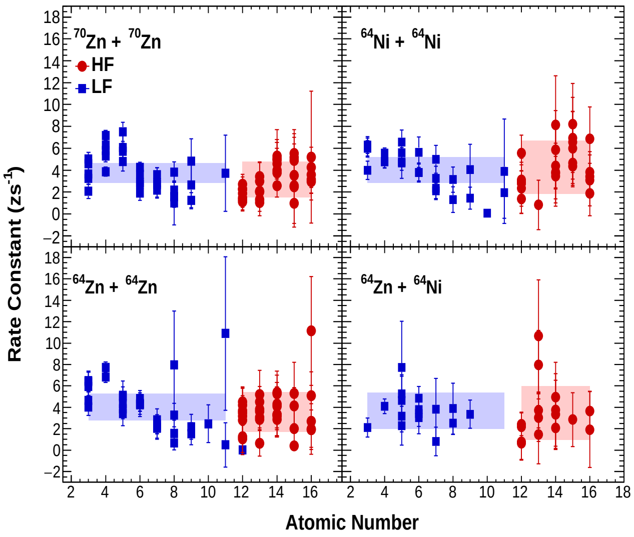

FIG. 14. Rate constants (in units of inverse zs) as a function of the atomic number. All four systems are represented: ^{70}Zn +^{70}Zn (top left panel), ^{64}Ni +^{64}Ni (top right panel), ^{64}Zn +^{64}Zn (lower left panel) and ^{64}Zn +^{64}Ni (lower right panel). The red circles represent the atomic numbers of the HF while the blue squares represent the atomic numbers LF. The shaded areas correspond to the average rate constant per zs values for the HF and LF. (color online)

stant per degree for the LF is 0.02 ± 0.01 and for the HF is 0.01 ± 0.02. It is reasonable to expect that the rate constants should be the same across different systems, since the rate constant ought to depend on the details of the nuclear equation of state, but not on the composition of the system or the chemical potentials involved.

The time scale is determined as in [22] using the angular distribution and assuming that the decay occurs in a fraction of the rotation time scale, as t=α/ω. The time is t and ω is the angular frequency, dependent on the angular momentum, J, and moment of inertia $I_{\rm eff}$ as ω=$(J\hbar)/I_{\rm eff}$. The J is assessed using GEMINI++ model, while the $I_{\rm eff}$ is calculated using a two touching spheres model, HF and LF, revolving around their common center of mass. Figure 14 shows the rate constants (in units of inverse zeptoseconds) as a function of the atomic number for all four systems studied for the LF (blue squares) and the HF (red circles). The equilibration rate constants for LF show a generally decreasing trend as Z increases up to Z=8. This could indicate that the equilibration process occurs more slowly for larger LF (i.e. a more mass-symmetric split of the PLF*); it is not obvious what the physical origin of this might be. This trend could also be symptomatic of a systematic error in the calculation of the moment of inertia which is exacerbated for small Z_L. The time scales for the full rotational period ranged from 1 to 4zs (i.e. 1zs=10^{-21}s=$300 fm/c$). The average rate constant per zs (represented in the figure as shaded areas) is, for the HF and the LF 4 ± 2 and 4 ± 1 zs^{-1}, respectively.

IV. SUMMARY

This work studies the time-dependence of neutron-proton equilibration in dynamically deformed nuclear systems by examining the composition of fragments produced by a system out of equilibrium. We employ a method to measure the equilibration's time evolution by studying the fragments produced from the PLF* in semi-peripheral collisions at 35 MeV per nucleon as a function of the breakup alignment angle. The alignment angle serves effectively as a clock for equilibration. The variation of the composition as a function of the alignment angle clock shows an exponential behavior simultaneously for both the light and the heavy fragments, suggesting first-order kinetics for all the systems studied. The yield and measured composition are used to extract an estimate for the purely dynamical component (unencumbered by statistical background). No modification of our extracted equilibration rate constants is warranted by the statistical background. Comparison to a statistical model indicates that our assessment of the equilibration rate constants is robust with respect to secondary decay. A small systematic effect in the composition is observed for reactions of a relatively neutron poor projectile with a neutron-rich target, consistent with physical expectations and a previous observation. No significant differences in the rate constants are noted between systems of different initial composition.

ACKNOWLEDGMENTS

This work is supported by the Robert A. Welch Foundation (Grant A-1266) and the U.S. Department of Energy DOE (Grant DE-FG02-93ER40773). We are thankful to the staff at the Texas A&M University Cyclotron Institute for providing the excellent quality beams and technical support that made this work possible.

[1] M. Tsang *et al.*, Phys. Rev. Lett. **92**, 062701 (2004).
[2] D. Shetty *et al.*, Phys. Rev. C **76**, 024606 (2007).
[3] Z. Sun *et al.*, Phys. Rev. C **82**, 051603 (2010).
[4] R. Planeta *et al.*, Phys. Rev. C **38**, 195 (1988).
[5] Bao-An and C. M. Ko, Phys. Rev. C **57**, 2065 (1998).
[6] E. Galichet *et al.*, Phys. Rev. C **79**, 064614 (2009).
[7] E. Galichet *et al.*, Phys. Rev. C **79**, 064615 (2009).
[8] C. Horowitz *et al.*, J. Phys. G **41**, 093001 (2014).

[9] A. Poulsen, oxidantshappencomics.wordpress.com.

[10] D. Theriault *et al.*, Phys. Rev. C **74**, 051602 (2006).

[11] B. Davin *et al.*, Phys. Rev. C **65**, 064614 (2002).

[12] J. Galin *et al.*, Z. Physik A **278**, 347 (1976).

[13] J. Kratz *et al.*, Phys. Rev. Lett. **39**, 984 (1977).

[14] L. Moretto and R. Schmitt, Rep. Prog. Phys. **44**, 533 (1981).

[15] E. Hernandez *et al.*, Nuc. Phys. A **361**, 483 (1981).

[16] G. Matthews *et al.*, Phys. Rev. C **25**, 300 (1982).

[17] H. Freisleben and J. Kratz, Phys. Rep. **106**, 1 (1984).

[18] S. Hudan *et al.*, Phys. Rev. C **86**, 021603 (2012).

[19] K. Brown *et al.*, Phys. Rev. C **87**, 061601 (2013).

[20] K. Stiefel *et al.*, Phys. Rev. C **90**, 061605 (2014).

[21] S. Hudan *et al.*, Eur. Phys. J. A **50**, 36 (2014).

[22] A. Jedele *et al.*, Phys. Rev. Lett **118**, 062501 (2017).

[23] S. Wuenschel *et al.*, NIMA **604**, 578 (2009).

[24] Z. Kohley *et al.*, Phys. Rev. C **82**, 064601 (2010).

[25] Z. Kohley, Ph.D. thesis, Texas A&M University (2010).

[26] C. Montoya *et al.*, Phys. Rev. Lett. **73**, 3070 (1994).

[27] J. Colin *et al.*, Phys. Rev. C **67**, 064603 (2003).

[28] E. D. Filippo *et al.*, Phys. Rev. C **71**, 044602 (2005).

[29] E. D. Filippo *et al.*, Phys. Rev. C **86**, 014610 (2012).

[30] A. McIntosh *et al.*, Phys. Rev. C **81**, 034603 (2010).

[31] A. McIntosh, Ph.D. thesis, Indiana University (2010).

[32] R. Charity, Phys. Rev. C **58**, 1073 (1998).